THE JOURNAL OF PHYSICAL CHEMISTRY C

ARTICLE

pubs.acs.org/JPCC

Electrochemical Growth of Gold Nanostructures for Surface-Enhanced Raman Scattering

Yu-Cheng Yang,[†] Ting-Kai Huang,[†] Yu-Liang Chen,[†] Jean-Yves Mevellec,[§] Serge Lefrant,[§] Chi-Young Lee,[‡] and Hsin-Tien Chiu*[,†]

[†]Department of Applied Chemistry, National Chiao Tung University, Hsinchu, Taiwan, 30050, Republic of China

[‡]Department of Materials Science and Engineering and Center for Nanotechnology, Materials Science, and Microsystems, National Tsing Hua University, Hsinchu, Taiwan, 30043, Republic of China

[§]Institut des Matériaux Jean Rouxel (IMN), Université de Nantes, CNRS, 44322 Nantes, France

Supporting Information

ABSTRACT: We demonstrate a facile fabrication of gold nanostructures including Au nanoplates (NPs), Au nanothorns (NTs), and Au nanowires (NWs) on indium tin oxide substrates via electrochemical growth. A simple two-electrode electrochemical deposition system was applied for the fabrication process. Dense Au nanostructures were grown directly on an Au seeding layer on the substrate. After 48 h, the Au NPs were 2−5 μm in width and 150−200 nm in thickness. The Au NTs were 1−3 μm in height, 300−500 nm in bottom side width, and 20 nm at the apex. The Au NWs were 30−80 nm in diameter and about 20 μm in length. The entire process was template-free and economical. We investigated the correlation between surface plasmon resonance (SPR) and surface enhanced scattering (SERS) effects of the Au nanostructures with different excitation wavelengths. By using the SPR absorption maxima of the nanostructures as the excitation wavelengths for SERS, the highest SERS enhancements were achieved. SERS effects of the Au NWs were investigated further. We discovered that the length and the density of the Au NWs affected the SERS performance significantly. The result is rationalized by the amount of "hot spot" generated at the crossing of the Au NWs. With the Au NWs, Rhodamine 6G can be detected at a concentration as low as 10^{-9} M.

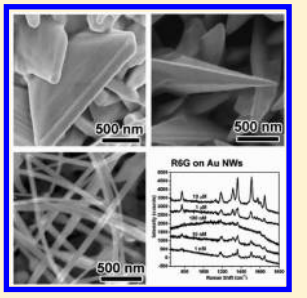

1. INTRODUCTION

Raman spectroscopy has proved to be a powerful tool for analytical applications.[1] Surface-enhanced Raman scattering (SERS) was first observed by Fleischman et al. in 1974.[2] It raised lots of interest with regard to fundamental studies and practical applications of the phenomenon in the following decades. The spectroscopy has been developed as a powerful tool to detect molecules adsorbed on SERS-active substrates. The merits of SERS are attributed to possible ultralow detection limits and intrinsic specificity of target molecules. In general, there are two possible enhancement mechanisms: electromagnetic effect and charge-transfer effect.[3,4] In many cases, the SERS phenomenon may be the result of cooperative effects of both mechanisms. Correlations between SERS and surface plasmon resonance (SPR) have been studied and connected both theoretically and experimentally.[5−7] SPR is the collective oscillation of conduction electrons on the surface of metal nanostructures.[8] SPR can be considered as an optical phenomenon of the nanomaterials. Morphology and size of the nanomaterials are important factors influencing the SPR wavelengths. In addition, optimizing the correlation between the SPR of the substrate and the excitation wavelength provides an efficient way to increase SERS performance.[9]

Researchers have been interested in maximizing SERS signals for facile and efficient analytical sensing applications. In experiments, the material and its morphology have been found to be the most crucial factors for highly sensitive SERS-active substrates. Nanostructures of Cu, Ag, Au, and Pt were discovered to provide good enhancements for SERS experiments.[10−13] The examples also included nanostructures of nanopores, nanogaps, nanoflowers, nanoparticle aggregates, nanowires, and nanorods.[13−19] In the vicinity of these unique nanostructures, SERS "hot spots" were created from gaps, pores, and slits when appropriate excitation wavelengths were used. Since the amounts of hot spots affect the SERS performance proportionally, all SERS-active substrates are designed to have high local electrical field enhancement and high amounts of hot spots.[20] Many of them are created by a semiconductor manufacturing process, such as lithography.[21] The advantages of the process are that uniform product morphology and reproducible fabrications can be achieved. On the other hand, the cost for fabricating each substrate may not be economical. In this study, we will show a facile fabrication of Au nanostructures including Au nanoplates (NPs), Au nanothorns (NTs), and Au nanowires (NWs) on indium tin oxide (ITO) substrates via a simple electrochemical growth process. We will report the correlation between the SPR and the SERS effects of the Au nanostructures with different excitation wavelengths. In addition, investigation on the SERS effects of the Au NWs will be discussed further. We have discovered that the SERS performances of the

Received: August 5, 2010
Revised: October 25, 2010
Published: January 5, 2011

nanostructures fabricated in this study are superior to the commercial SERS-active substrate Klarite. Our discoveries are reported below.

2. RESULTS AND DISCUSSION

Recently, we reported a simple surfactant-assisted growth of Au NWs via a galvanic reduction route.[22] Here, we extend the process to a straightforward dc electrodeposition procedure, employing a two-electrode system shown in Figure S1 (Supporting Information), so that more growth factors can be controlled. In the reaction, in the presence of cetyltrimethylammonium chloride (CTAC) and $NaNO_{3(aq)}$, $AuCl_4^-{}_{(aq)}$ ions were reduced and deposited on the surface of an ITO cathode coated sequentially with a layer of sputtered Ti and a layer of sputtered Au, as shown in the scanning electron microscopic (SEM) image in Figure S2A (Supporting Information). The Au layer (Figure S2B in the Supporting Information) served as a seeding layer for Au nucleation.[23−25] By controlling the growth parameters, as shown in Table S1 (Supporting Information), we obtained a series of nanostructures, including NPs, NTs, and NWs on the ITO substrates. Since the reduction of an $AuCl_4^-{}_{(aq)}$ ion into a solid state Au atom requires three electrons, the total amount of Au deposited on the substrate can be measured quantitatively from the quantity of electrons supplied, by integrating the electric current delivered against the deposition time. The voltage applied across the cathode and the anode played a crucial role in the electrochemical deposition. It not only provided a driving force for the reduction but also acted as one of the key factors influencing the reaction rate and the product morphology. As shown by the energy dispersive spectra (EDS) in Figure S3 (Supporting Information), all of the deposited solids were characterized to be Au. When 3.0 V was applied, the reduction was rapid and aggregates of irregular clusters formed (Figure S3A in the Supporting Information). As lower voltages were applied, not only the growth rates decreased but more anisotropic growths of nanomaterials were observed (Figure S3B,C in the Supporting Information). When 0.7 V was used, a rodlike nanostructure appeared, as shown in Figure S3D (Supporting Information). On the basis of the observation, we anticipate that the growth of Au nanostructures should be more controllable at this voltage. As reported in the literature, the surfactant concentration affected crystal growths significantly.[25] Next, we fixed the concentrations of $HAuCl_{4(aq)}$ and $NaNO_{3(aq)}$ but altered the CTAC concentration in a series of experiments. The effect of the CTAC concentration on the Au morphology is shown in Figure S4 (Supporting Information). As the CTAC concentration increased from 1.8 to 9.0 mM, deposition of the Au structures shifted toward more anisotropic growth, from Au NPs (CTAC, 1.8 mM) to Au NTs (CTAC, 3.2 mM) and finally to Au NWs (CTAC, 9.0 mM). A representative XRD pattern shown in Figure S5 (Supporting Information) also confirmed that the deposited solids were $Au_{(s)}$.

2.1. Characterization of Gold Nanostructures. Figure 1 shows the low and high magnification SEM images of the Au nanostructures on the substrates after deposited for 48 h. Panels A and B of Figure 1 display the images of the randomly grown Au NPs. The width and height of each Au NP are about 2−5 μm while the thickness is 150−200 nm. Images in panels C and D of Figure 1 reveal that each of the Au NTs has a height 1−3 μm, a side width 300−500 nm at the bottom, and a tip about 20 nm at the apex. Panels E and F of Figure 1 show that the substrate is densely covered by Au NWs with diameters 30−80 nm and lengths up to 20 μm. As shown in Figure S6 (Supporting Information), the Au NWs grew directly on the seed layer on the Au−Ti−ITO substrate.

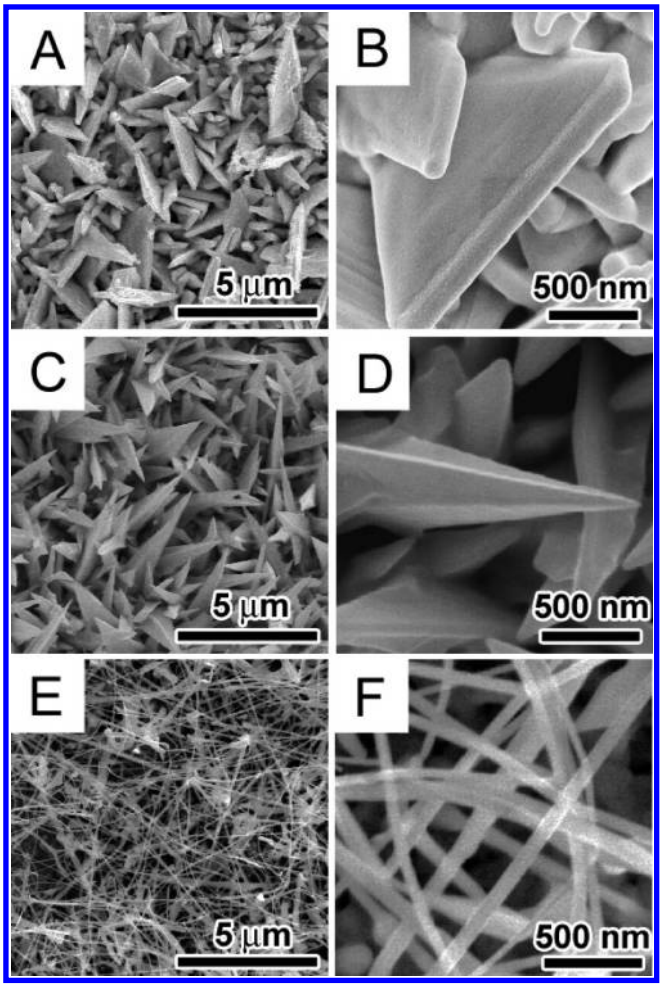

Figure 1. Low- and high-magnification SEM images: (A and B) Au NPs; (C and D) Au NTs; (E and F) Au NWs.

Figure 2 shows the transmission electron microscopy (TEM) studies of an irregularly shaped Au NP (Figure 2A). Figure 2B displays its electron diffraction (ED) pattern. According to the pattern, we conclude that the Au NP is composed of face-centered cubic (fcc) crystals. The high-resolution TEM (HRTEM) images in panels C and D of Figure 2, taken from the locations pointed by the arrows shown in Figure 2A, clearly indicate that each of the locations is single crystalline. The images correspond well to the [011] crystallographic zone axis of the fcc structure. The *d*-spacing measured from the fringes in the images is 0.23 nm, close to the *d*-spacing of Au {111} planes (JCPDS 04-0784).[26] From the ED and the HRTEM results, the lattice parameter *a* is calculated to be 0.41 nm. This is consistent with the value of Au, 0.407 nm. TEM studies of a representative Au NT are shown in Figure 3. The low-magnification image (Figure 3A) indicates that the structure has a length of 800 nm, a projected bottom width of 250 nm, and a sharp tip. On the basis of the dot ED pattern shown in Figure 3B, the NT is determined to be an fcc single crystal. The image corresponds to the [1−1−2] crystallographic zone axis, indicating that the Au NT grew along the [110] direction. From the area pointed by an arrow in the high-magnification image in Figure 3C, an HRTEM image is taken and displayed in Figure 3D. The *d*-spacing estimated from the fringes in Figure 3D is 0.23 nm, again close to the *d*-spacing of Au {111} planes. The lattice parameter *a* is calculated to be

dx.doi.org/10.1021/jp1073544 |J. Phys. Chem. C 2011, 115, 1932–1939

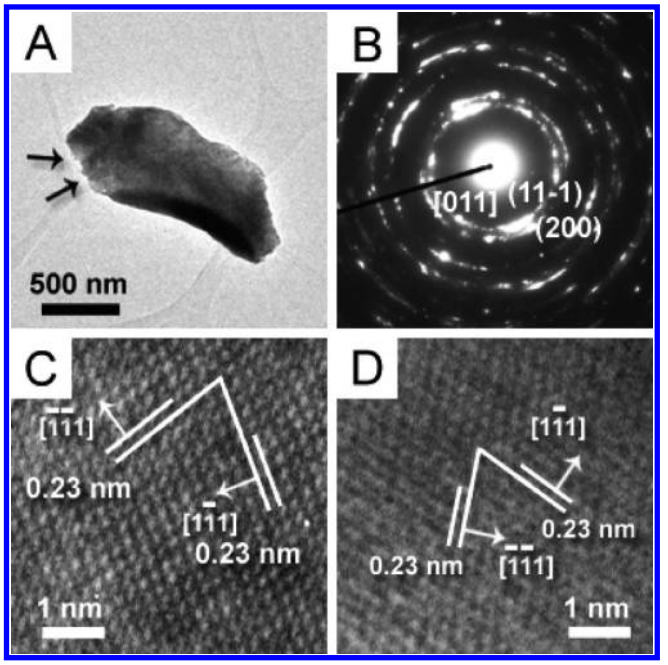

Figure 2. TEM studies of an Au NP: (A) low-magnification image and (B) ED pattern; (C and D) HRTEM images of two different areas pointed by the arrows in (A).

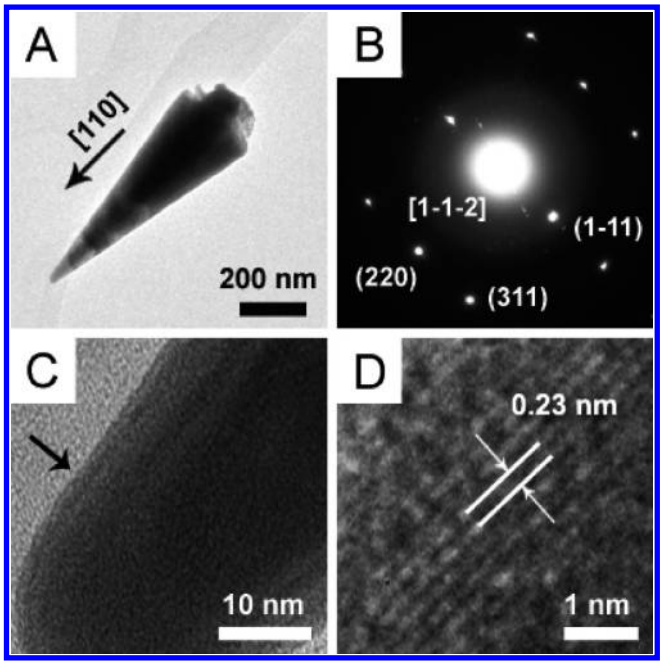

Figure 3. TEM studies of an Au NT: (A) low-magnification image and (B) ED pattern; (C) high-magnification image and (D) HRTEM image of the area pointed by the arrow in (C).

0.41 nm, also consistent with the value of Au, 0.407 nm. The TEM studies of a representative Au NW are shown in Figure 4. The low-magnification image (Figure 4A) confirms that the material has a uniform wire structure with a diameter 30 nm. The dot ED pattern shown in Figure 4B reveals that it has a single crystalline fcc structure. The pattern corresponds to the [−111] crystallographic zone axis, suggesting that the Au NW growth was along the [110] direction. Figure 4D shows the HRTEM

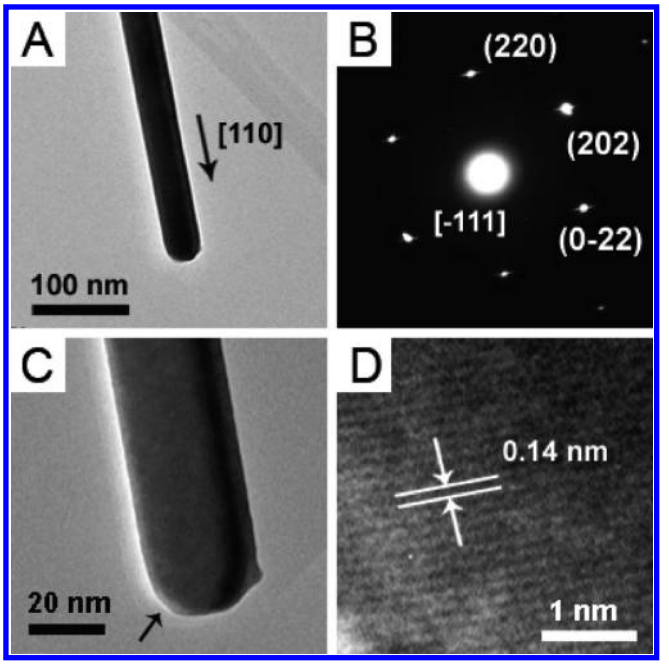

Figure 4. (A) Low-magnification TEM image of an Au NW, (B) SAED pattern, (C) high-magnification TEM image of the Au NW shown in (A), and (D) HRTEM image of the indicated region in (C).

Scheme 1. Proposed Growth Mechanism of Gold Nanostructures

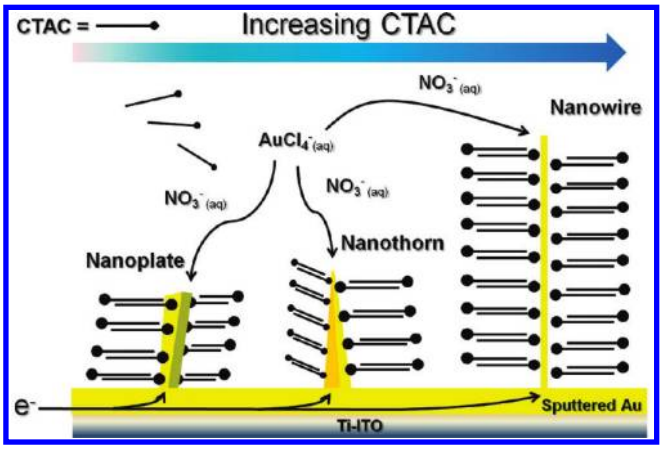

image of the area pointed by an arrow in the high-magnification TEM image in Figure 4C. The *d*-spacing determined from the fringes is 0.14 nm. It agrees well with the *d* spacing of Au {110} planes. The calculated lattice parameter *a* is 0.41 nm. Again, it is close to the value of Au, 0.407 nm.

2.2. Proposed Growth Mechanism. We proposed following pathway, as summarized in Scheme 1, to rationalize the observed nanostructure growths. Initially, the sputtered Au layer on the substrate acts as the seeds for the Au nucleation. This step parallels the homogeneous solution phase nucleation mechanism proposed by Murphy's group.[25] The growth temperature and the applied voltage are lowered to prevent fast uncontrolled $Au_{(s)}$ deposition. In many investigations, an adequate quantity of surfactant has been added for possible shape control of the fabrication of 1D nanomaterials.[22,27,28] The surfactant CTAC

Table 1. Real Surface Areas and Roughness Factors

sample	RSA (cm^2)	deposited weight (μg)	specific RSA (cm^2/g)	RF
sputtered Au	0.265	not measured	not estimated	0.94
Au NPs	5.245	2166	2421	18.60
Au NTs	3.690	1521	2426	13.09
Au NWs	1.410	50	28143	5.00

added in this study not only lowers the surface energy of the as-deposited $Au_{(s)}$ but also acts as a capping agent.[29] The cationic surfactant molecules probably adsorb selectively on preferred low-index facets, such as Au{100} and Au{111}. This would suppress random growth so that specific product morphology can be obtained. With more CTAC, more crystal surfaces would be covered so that the structures change from NP to NT and finally into NW. The presence of $NO_3^-{}_{(aq)}$ ions in the growth solution is another determinant for controlling the crystal shape in the system. The function of the ions may resemble their role in aqua regia, well-known for its ability to oxidize $Au_{(s)}$ into $AuCl_4^-{}_{(aq)}$ ions.[30] During the crystal growth, the less stable facets might be oxidized by $NO_3^-{}_{(aq)}$ easily, leaving the more stable facets exposed for further developments. As a result, all these factors function cooperatively in the electrochemical deposition to direct the crystals to grow into the observed morphology.

2.3. Real Surface Area and Roughness Factor of Gold Nanostructures. Real surface areas (RSAs) of the Au nanostructures were characterized by cyclic voltammetry (CV) in $H_2SO_{4(aq)}$ (Figure S7 in the Supporting Information).[31] The anodic current started at 1.1 V was due to the formation of gold oxide. Subsequently, the oxide was reduced in the negative potential scan began at about 1 V. By integrating the reduction current of the gold oxide formed in the positive scan, the RSAs were calculated by assuming that the reduction of a monolayer of Au oxide requires $390 \pm 10\,\mu C\ cm^{-2}$.[32] We also recorded the reduction currents used during the electrodeposition process (Figure S8 in the Supporting Information) and converted the consumed charges into the weights of the deposited Au nanostructures. Both of the RSA and the deposited weight of each sample are listed in Table 1. Compared to the deposited weights of the Au NPs and the Au NTs, the value of the Au NWs is extremely low. We attribute the low deposition rate to the presence of a high concentration of CTAC in the growth solution. The excess amount of the surfactant molecules would occupy more of the growth sites and slow down the Au deposition. To compare the surface area of exposed Au atoms per a unit weight of deposited $Au_{(s)}$, we estimated the specific RSA, in $cm^2\ g^{-1}$, and listed it in Table 1 for each sample. Even though the Au NPs and the Au NTs show high RSAs, the Au NWs present the highest specific RSA. This is due to the high aspect ratio of the 1D nanostructure which allows more Au atoms to expose on the surface. Also, we calculated the roughness factor (RF), the RSA divided by the geometrical area, for each sample. The results are listed in Table 1. The sputtered Au has an RSA of 0.265 cm^2, which is close to its geometric area, 0.282 cm^2. Consequently, its RF is 0.94, close to 1. The other electrochemically deposited Au samples show RFs ranged from 5.00 for the NWs to 18.60 for the NPs.

2.4. Correlation of Surface Plasmon Resonance and Surface-Enhanced Raman Scattering of Gold Nanostructures. We are interested in correlating the surface plasmon resonance (SPR) to the surface-enhanced Raman scattering (SERS) for each Au nanostructure. Figure 5A shows the extinction spectra of the nanostructures. The absorption maxima are observed at 514 nm for the Au NPs, at 530 nm for the Au NTs, and at 494 nm

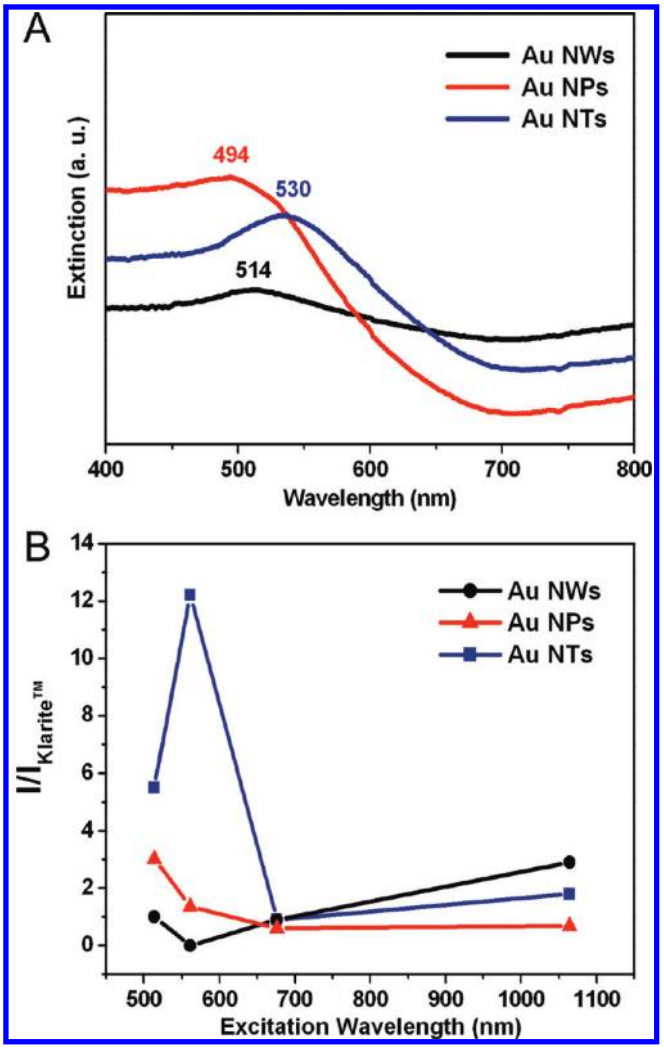

Figure 5. (A) UV−vis extinction spectra of Au NWs (black), Au NPs (red), and Au NTs (blue). (B) Effect of excitation wavelengths on ratios of SERS intensities of *trans*-stilbene (1594 cm^{-1}) on Au nanostructures (NWs (black), NPs (red), NTs (blue)) and on Klarite substrate.

for the Au NWs. Furthermore, the Au NWs show extended absorption into long wavelengths, probably originated from the low frequency longitudinal absorption of the 1D nanostructure. Figure S9 in the Supporting Information showed a series of SERS spectra of *trans*-stilbene (*t*SB) on the Au samples prepared in this study. For comparison, we also used a commercial SERS-active Klarite substrate (Figure S10 in the Supporting Information) as the reference for our investigation. Excitation wavelengths 514, 561, 676, and 1064 nm were employed for the SERS measurements. In general, four major *t*SB vibrations were observed at 1002, 1198, 1594, and 1639 cm^{-1} in Figure S9 (Supporting Information).[33] They corresponded well to the Raman signals of a bulk *t*SB solid. The assignments are listed in Table S2 in the Supporting Information. Clearly, the randomly distributed gaps, slits, vacancies, and crossings on the Au nanostructures provided "hot spots" for electromagnetic (EM) field enhancements.[34,35] For comparison of the effectiveness of various Au nanostructures, we used the intensity of the *t*SB signal at 1594 cm^{-1} on Klarite as the reference. Then the ratio of the intensities of *t*SB on the Au nanostructure and on Klarite is calculated and plotted against the excitation wavelengths in Figure 5B. With the proper

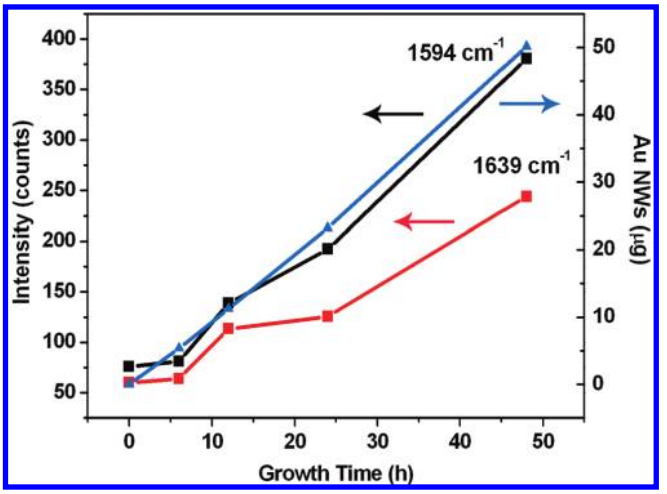

Figure 6. Correlation between SERS intensities of *t*SB (black, 1594 cm^{-1}; red, 1639 cm^{-1}) and Au NWs growth time. The blue line represents the amount of deposited Au NWs (calculated from the electric charges applied).

selection of an excitation wavelength near the SPR maximum of each nanostructure shown in Figure 5A, the *t*SB signal can be enhanced several fold over the one taken on Klarite. With the maximum SPR at 494 nm, the Au NPs display the highest *t*SB signal enhancement when the molecule is excited at 514 nm. The Au NTs show 5-fold and 12-fold enhancements over Klarite, at 514 and 561 nm, respectively. Both excitation wavelengths are close to the maximum SPR absorption of the Au NTs at 530 nm. The Au NWs show better enhancements at the excitation wavelengths 514 and 1064 nm. This is consistent with the SPR result, which displays a maximum absorption at 514 nm and an enhanced longitudinal absorption above 800 nm.

2.5. Surface-Enhanced Raman Scattering of Gold Nanowires. From the results discussed above, we found that the Au NWs performed well as a SERS material. Compared to the deposition of the other Au nanostructures fabricated in this study, only a limited amount of $Au_{(s)}$ is needed to grow the NWs. Another advantage is that the growth is a simple, hard-template-free process.[36] Thus, we decide to investigate the Au NWs for SERS applications further. As mentioned in the literature, enhanced plasmon resonance could be generated near the vicinity of the crossing of NWs.[37,38] As a result, the crossings could act as SERS hot spots. To test this theory, we grew a series of Au NWs with different growth times. As shown in the SEM images in Figure S11 in the Supporting Information, both the density and the length of the NWs increased with the increasing growth time. Figure S12 (Supporting Information) displays the SERS signals of *t*SB on the Au NWs shown in Figure S11 (Supporting Information). Clearly, the Raman signals enhanced more by the Au NWs with longer growth time. Figure 6 summarizes the correlation between the amount of the deposited $Au_{(s)}$ and the SERS intensities of the *t*SB vibrations at 1594 and 1639 cm^{-1}. As the growth time increases, both of them increase proportionally. This can be rationalized by the following reasons. As the length and the density of the Au NWs on the substrate increase, the density of the hot spots generated by the crossings increases as well. Consequently, the SERS intensities are enhanced by the increased number of hot spots. In Scheme 2, we show a model to illustrate the relationship between the number of hot spots and the density of NW crossings. The SEM images in Figure 7 display examples of the Au NW crossings overlaying on the

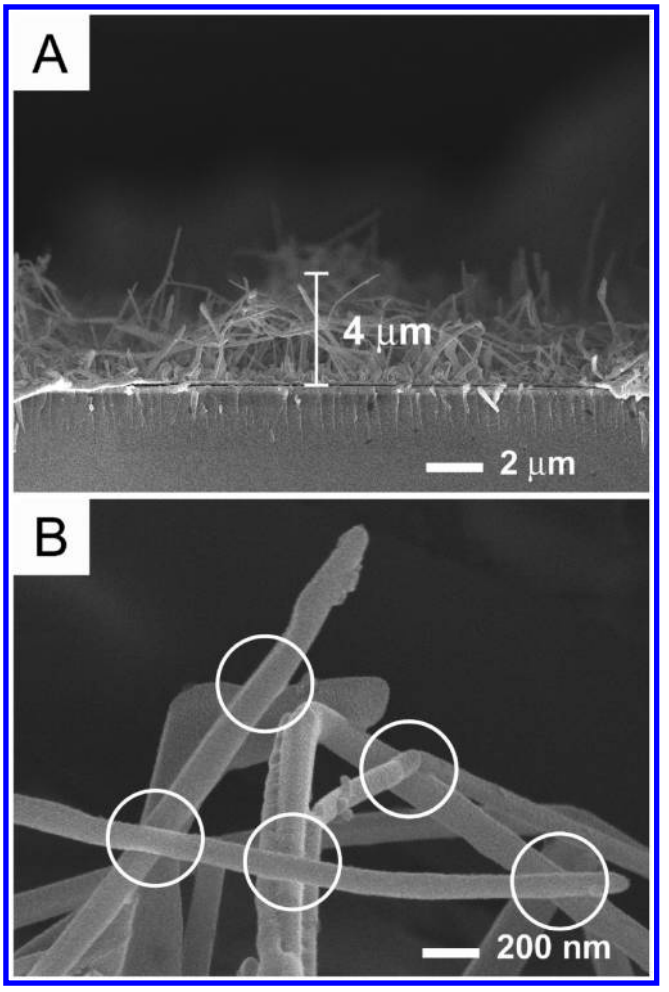

Figure 7. (A) Low and (B) high magnification side-view images of Au NWs on substrate. White circles mark the crossings.

Scheme 2. Proposed Hot Spot Formation Mechanism

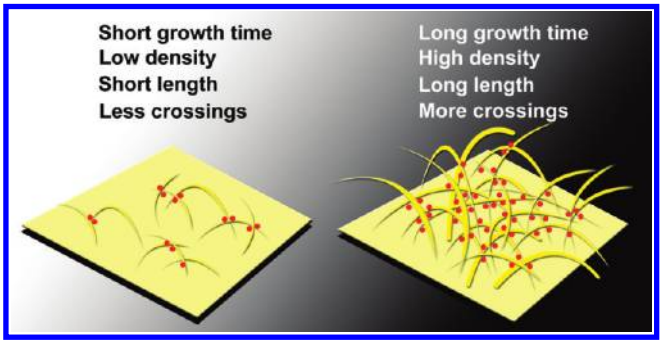

substrate. We also carried out Raman mapping studies employing Rhodamine 6G (R6G), a molecule with large Raman scattering cross section, as the probe molecule to determine the influence of the Au NW crossing densities in an area 50 μm × 50 μm. The images shown in Figure S13 (Supporting Information) confirmed that the longer and higher density Au NWs (grown for 48 h) provided not only higher signal intensities but also more uniform enhancements than the shorter and lower density NWs (grown for 6−24 h) did. More observations related to R6G sensing will be discussed below.

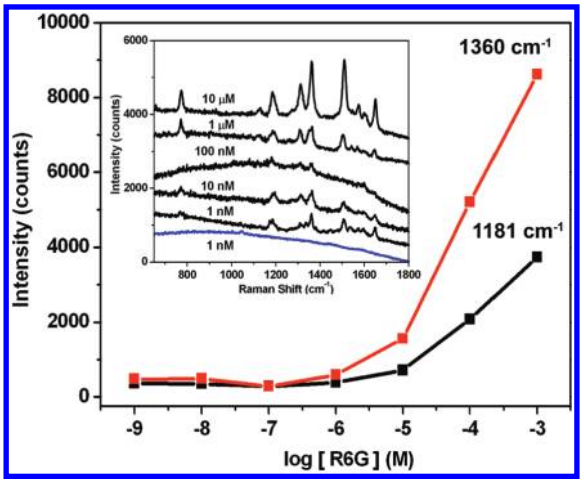

Figure 8. SERS intensities of various R6G concentrations (in ethanol, 10 μL; black square, 1181 cm^{-1}; red square, 1360 cm^{-1}). Inset: the SERS spectra of different concentrations of R6G on Au NWs substrate (black) and Klarite (blue).

On the Au NWs grown for 48 h, a series of SERS experiments using an excitation wavelength of 632.8 nm were carried out to test the detection limit of R6G on the substrate. The SERS responses of the R6G vibrations at 1181 and 1360 cm^{-1} versus the concentration of the molecule are shown in Figure 8. Clearly the SERS intensities increase with the increasing R6G concentrations. The signals observed at 770, 1181, 1309, 1360, 1508, 1571, and 1647 cm^{-1} are assigned to the R6G vibrational frequencies calculated by Schatz et al.[39] The assignments are listed in Table S3 in the Supporting Information. The SERS signals from R6G (1 nM) on the Au NWs are shown in the inset of Figure 8. All of the major R6G vibration signals can be observed clearly. For comparison, adding the same R6G concentration on Klarite does not generate a meaningful SERS response. Figure S14 (Supporting Information) shows the SERS spectra from ultralow concentrations, 100 and 1 fM, of R6G on the Au NWs and Klarite. Even at these concentrations, some Raman signals were still detected on the Au NWs. Peaks at 1475 and 1546 cm^{-1} were observed when the concentration of R6G was down to 100 fM. Also, peaks at 1488 and 1581 cm^{-1} were still visible when the concentration of R6G was lowered further to 1 fM. Other characteristic R6G vibrations, such as the ones at 1360 and 1508 cm^{-1}, diminished beyond possible detections. The lack of some signals may be attributed to specific orientations of R6G molecules adsorbed on the Au surface. In literature, it is found that the orientation of molecules on the surface affects the Raman intensities of specific vibrational modes strongly.[40] This is because certain modes, such as in-plane and out-of-plane vibrations, are highly influenced by the local electrical field parallel or perpendicular to the molecules.[40,41] Another possible reason is that when molecules are trapped in the hot spots, some physical stress may be generated so that the adsorbed molecules undergo certain structural transformations.[42]

2.6. Analytical Enhancement Factor of Gold Nanowires. Using the data in Figure S15 in the Supporting Information, the analytical enhancement factor (AEF), defined by the equation AEF = $(I_{SERS}/C_{SERS})/(I_{RS}/C_{RS})$, is estimated for the Au NWs grown for 48 h.[43] Here, I_{SERS} is the SERS intensity of R6G on the Au NWs. C_{SERS} is the concentration of the analyte. On the other hand, I_{RS} stands for the Raman intensity of R6G on a non-SERS active glass substrate. The concentration of R6G is C_{RS}. From the experimental data, the AEF of the Au NWs is calculated from the SERS intensities of R6G at 1360 and 1508 cm^{-1}. The average AEF value is about 10^5. This is comparable to the AEF of Klatrite.[44] As shown in the Raman mappings of an area 50 μm × 50 μm in Figure S16 (Supporting Information), the Au NWs provided more uniform enhancement of the R6G signal on the substrate surface than Klarite did.

3. CONCLUSION

In this study, we demonstrated the fabrication of a series of Au nanostructures on Au−Ti−ITO substrates via a simple electrochemical deposition process. When different voltages and CTAC concentrations are applied, three representative morphologies of Au nanostructures, including NPs, NTs, and NWs, were grown directly on the substrates. We estimated the RSAs and the RFs of the Au nanostructures using the results from the CV experiments. We discovered that even though the NPs and the NTs had higher RSAs, the NWs show the highest specific RSA, i.e., the NWs exposed more surface areas per unit amount of $Au_{(s)}$ deposited. This feature is attributed to the specific 1D structure of the NWs.

Furthermore, we investigated the SERS effects on these Au nanostructures by applying different excitation wavelengths to confirm the correlation between their SPR and the SERS results. The best excitation wavelengths for the SERS were found to be near the SPR absorption maxima of the nanostructures. Since the growth of the Au NWs consumed the least amount of $Au_{(s)}$, we investigated the material for potential SERS detection of molecules with low concentrations. R6G was employed as the probe molecule. We discovered that the presence of 1 nM of R6G on the AuNWs can be confidently observed. Detecting 1 fM of R6G appeared to be promising. This may be realized if the fabrication process can be optimized further. The AEF of the Au NWs was estimated to be 10^5. The enhancement was uniform over the substrate surface. We proposed a hot spot formation model to rationalize the observed high and uniform SERS enhancement by the Au NWs. The morphology of the NWs grown in this study provided high density extra long 1D nanostructures on the substrate. Consequently, a high density of Au NW crossings was created on the substrate to provide a large amount of hot spots. We anticipate that the low-cost, high-performance nanostructured Au substrates may be applied for rapid sensing applications in the future.

4. EXPERIMENTAL SECTION

4.1. Materials. ITO glasses (Sigma-Aldrich, indium tin oxide coated glass slide, surface resistance: 5−15 Ω/sq) were used as the growth substrates. $HAuCl_4 \cdot 3H_2O$ (Sigma Aldrich), CTAC (Taiwan Surfactant), and $NaNO_3$ (Riedel-de Haën) were used in the Au nanostructure fabrications. *t*SB (Sigma-Aldrich) diluted in pure diethyl ether (Sigma-Aldrich, ACS reagent, anhydrous, ≥ 99.0%) and R6G (Sigma-Aldrich) diluted in alcohol (Sigma-Aldrich, purity >99.5%) were used as the probe analytes for the SERS experiments.

4.2. Preparation of Growth Substrates. An ITO glass (0.5 cm ×2 cm) was precleaned with glass cleaner, deionized water, and acetone. Next, a Ti thin film (thickness, 30 nm), acting as an adhesion layer, was deposited on the ITO glass by an E-gun evaporation system (AST PEVA 600I). Then, an Au thin film (thickness, 50 nm) was sputtered on the Ti thin film by using an

auto sputter coater (PELCO SC-7). After annealing at 573 K under Ar atmosphere for 4 h, the substrate (shown in Figure S2 in the Supporting Information) provided improved adhesion between the ITO glass and the deposited Au nanostructures.[45]

4.3. Growth of Gold Nanostructures. Proper amounts of $HAuCl_4 \cdot 3H_2O$, CTAC, and $NaNO_3$ were mixed with deionized water to offer the growth solution. The concentration of each component and the growth condition are summarized in Table S1 (Supporting Information). After the mixture was sonicated for 5 min, it was placed in a cooling bath at 290 K. A simple two-electrode electrochemical deposition system shown in Figure S1 (Supporting Information) was used for the depositions. The Au−Ti−ITO substrate was used as the cathode while the anode was fabricated from a dried carbon paste on a transparent projection slide. After the growth solution was added into the system, a controlled electrical voltage was applied across the electrodes. After some time, growth of an Au nanostructure on the cathode surface was observed. Finally, we rinsed the sample with alcohol (Sigma-Aldrich, 97%) and deionized water before further investigations.

4.4. Instruments for Characterizations. The SEM images and the EDS data were taken from a Hitachi S-4000 (25 keV) and a JEOL JSM-7401F (15 keV). TEM, ED, and HRTEM images were captured by a JEOL JEM-3000F at 300 kV. XRD data were obtained from Bruker AXS D8 Advance.

4.5. Real Surface Area Measurements. Electrochemical measurements were carried out using an electrochemical analyzer (CH Instruments 6081C). The nanostructured Au substrates were used as the working electrodes. A Pt wire was employed as the counter electrode while an Ag|AgCl electrode was used as the reference electrode. All potentials were quoted relative to the Ag|AgCl reference. Electron-transfer properties of the Au electrodes were evaluated by using the CV results, carried out in $H_2SO_{4(aq)}$ (0.5 M, 20 mL). The RSAs of the electrodes were calculated from the corresponding currents of the voltammetric peaks shown in Figure S7 (Supporting Information).[31]

4.6. Spectroscopy Measurements. The UV−visible extinction spectra of the Au nanostructures were acquired from a spectrophotometer (Hitachi U-3010) in the reflection mode. The background of the substrate was subtracted for all of the spectra. The Raman spectra were acquired using a high-resolution confocal Raman spectrometer HORIBA LabRAM HR800 (excitation wavelength 632.8 nm) and a Jobin-Yvon T64000 (excitation wavelengths 514, 561, 676, and 1064 nm). Diluted *t*SB in pure diethyl ether and diluted R6G in pure alcohol were employed as the analytes. The analyte (10 μL) was dropped on the substrate for each measurement. The spectra recorded sequentially in experiments with the same instrumental settings were compared. The Raman mapping was carried out on an XY-stage using the excitation wavelength 632.8 nm.

■ ASSOCIATED CONTENT

Supporting Information. Tables of list of growth conditions and assignments of selected Raman peaks and figures showing a diagram of electrodeposition system, SEM and optical images, EDS data, an XRD pattern, variations of reduction current against time, CV diagrams, SERS data, and AEF calculations. This material is available free of charge via the Internet at http://pubs.acs.org.

■ AUTHOR INFORMATION

Corresponding Author
*E-mail: htchiu@faculty.nctu.edu.tw.

■ ACKNOWLEDGMENT

We thank the support from the National Science Council, "Aim for the Top University Plan" of the National Chiao Tung University, and the Ministry of Education of Taiwan, the Republic of China. Also, we thank Professors Kien-Wen Sun, Shinsuke Shigeto, and Ian Liau for experimental assistance.

■ REFERENCES

(1) Adler-Golden, S. M.; Goldstein, N.; Bien, F.; Matthew, M. W.; Gersh, M. E.; Cheng, W. K.; Adams, F. W. *Appl. Opt.* **1992**, *31*, 831.
(2) Fleischman, M.; Hendra, P. J.; McQuillan, A. *J. Chem. Phys. Lett.* **1974**, *26*, 163.
(3) Albrecht, M. G.; Creighton, J. A. *J. Am. Chem. Soc.* **1977**, *99*, 5215.
(4) Jeanmaire, D. L.; Van Duyne, R. P. *J. Electroanal. Chem.* **1977**, *84*, 1.
(5) Moskovits, M. *Rev. Mod. Phys.* **1985**, *57*, 783.
(6) Haynes, C. L.; Van Duyne, R. P. *J. Phys. Chem. B* **2003**, *107*, 7426.
(7) Alvarez-Puebla, R.; Cui, B.; Bravo-Vasquez, J.-P.; Veres, T.; Fenniri, H. *J. Phys. Chem. C* **2007**, *111*, 6720.
(8) Moores, A.; Goettmann, F. *New J. Chem.* **2006**, *30*, 1121.
(9) Jackson, J. B.; Halas, N. J. *Proc. Natl. Acad. Sci. U.S.A.* **2004**, *101*, 17930.
(10) Wang, H.; Levin, C. S.; Halas, N. J. *J. Am. Chem. Soc.* **2005**, *127*, 14992.
(11) Richard, J. C. B.; Martin, J. T. M. *J. Raman Spectrosc.* **2008**, *39*, 1313.
(12) Wang, T.; Hu, X.; Dong, S. *J. Phys. Chem. B* **2006**, *110*, 16930.
(13) Sawai, Y.; Takimoto, B.; Nabika, H.; Ajito, K.; Murakoshi, K. *J. Am. Chem. Soc.* **2007**, *129*, 1658.
(14) Qian, L. H.; Yan, X. Q.; Fujita, T.; Inoue, A.; Chen, M. W. *Appl. Phys. Lett.* **2007**, *90*, No. 1531201.
(15) Duan, G.; Cai, W.; Luo, Y.; Li, Z.; Li, Y. *Appl. Phys. Lett.* **2005**, *89*, No. 2119051.
(16) Schwartzberg, A. M.; Grant, C. D.; Wolcott, A.; Talley, C. E.; Huser, T. R.; Bogomolni, R.; Zhang, J. Z. *J. Phys. Chem. B* **2004**, *108*, 19191.
(17) Billot, L.; Lamy de la Chapelle, M.; Grimault, A. S.; Vial, A.; Barchiesi, D.; Bijeon, J. L.; Adam, P. M.; Royer, P. *Chem. Phys. Lett.* **2006**, *422*, 303.
(18) Tao, A.; Kim, F.; Hess, C.; Goldberger, J.; He, R.; Sun, Y.; Xia, Y.; Yang, P. *Nano Lett.* **2003**, *3*, 1229.
(19) Orendorff, C. J.; Gearheart, L.; Jana, N. R.; Murphy, C. J. *Phys. Chem. Chem. Phys.* **2006**, *8*, 165.
(20) Wang, Z. B.; Luk'yanchuk, B. S.; Guo, W.; Edwardson, S. P.; Whitehead, D. J.; Li, L.; Liu, Z.; Watkins, K. G. *J. Chem. Phys.* **2008**, *128*, No. 094705.
(21) Wu, W.; Hu, M.; Ou, F. S.; Li, Z.; Williams, R. S. *Nanotechnology* **2010**, *21*, No. 2555021.
(22) Huang, T.-K.; Chen, Y.-C.; Ko, H.-C.; Huang, H.-W.; Wang, C.-H.; Lin, H.-K.; Chen, F.-R.; Kai, J.-J.; Lee, C.-Y.; Chiu, H.-T. *Langmuir* **2008**, *24*, 5647.
(23) Wu, H.-L.; Chen, C.-H.; Huang, M. H. *Chem. Mater.* **2008**, *21*, 110.
(24) Kumar, S.; Yang, H.; Zou, S. *J. Phys. Chem. C* **2007**, *111*, 12933.
(25) Murphy, C. J.; Jana, N. R. *Adv. Mater.* **2002**, *14*, 80.
(26) Joint Committee for Powder Diffraction (JCPDS) File No. 04-0784. International Center for Diffraction Data, 1953.
(27) Johnson, C. J.; Dujardin, E.; Davis, S. A.; Murphy, C. J.; Mann, S. *J. Mater. Chem.* **2002**, *12*, 1765.
(28) Nikoobakht, B.; El-Sayed, M. A. *Chem. Mater.* **2003**, *15*, 1957.
(29) Nikoobakht, B.; El-Sayed, M. A. *Langmuir* **2001**, *17*, 6368.
(30) Raptis, R. G.; Fackler, J. P. *Inorg. Chem.* **1990**, *29*, 5003.
(31) Xiang, C.; Guell, A. G.; Brown, M. A.; Kim, J. Y.; Hemminger, J. C.; Penner, R. M. *Nano Lett.* **2008**, *8*, 3017.
(32) Trasatti, S.; Petrii, O. A. Real Surface Area Measurements in Electrochemistry. *Pure Appl. Chem.* **1991**, *63*, 711.
(33) Choi, C. H.; Kertesz, M. *J. Phys. Chem. A* **1997**, *101*, 3823.
(34) Qin, L.; Zou, S.; Xue, C.; Atkinson, A.; Schatz, G. C.; Mirkin, C. A. *Proc. Natl. Acad. Sci. U.S.A.* **2006**, *103*, 13300.

(35) Chen, C.; Hutchison, J. A.; Clemente, F.; Kox, R.; Uji-I, H.; Hofkens, J.; Lagae, L.; Maes, G.; Borghs, G.; Van Dorpe, P. *Angew. Chem.* **2009**, *121*, 10116.
(36) Lee, S. J.; Morrill, A. R.; Moskovits, M. *J. Am. Chem. Soc.* **2006**, *128*, 2200.
(37) Prokes, S. M.; Alexson, D.; Glembocki, O. J.; Park, H. D.; Rendell, R. W. *J. Vac. Sci. Technol., B* **2009**, *27*, 2055.
(38) Prokes, S. M.; Glembocki, O. J.; Rendell, R. W.; Ancona, M. G. *Appl. Phys. Lett.* **2007**, *90*, No. 0931051.
(39) Jensen, L.; Schatz, G. C. *J. Phys. Chem. A* **2006**, *110*, 5973.
(40) Cai, W.-B.; Wan, L.-J.; Noda, H.; Hibino, Y.; Ataka, K.; Osawa, M. *Langmuir* **1998**, *14*, 6992.
(41) Ru, E. C. L.; Meyer, M.; Blackie, E.; Etchegoin, P. G. *J. Raman Spectrosc.* **2008**, *39*, 1127.
(42) Chen, T.; Wang, H.; Chen, G.; Wang, Y.; Feng, Y.; Teo, W. S.; Wu, T.; Chen, H. *ACS Nano* **2010**, *4*, 3087.
(43) Ru, E. C. L.; Blackie, E.; Meyer, M.; Etchegoin, P. G. *J. Phys. Chem. C* **2007**, *111*, 13794.
(44) D3 Technologies Inc., Klarite The Gold Standard in SERS Substrates. http://www.renishawdiagnostics.com/en/klarite--12409.
(45) Hoogvliet, J. C.; van Bennekom, W. P. *Electrochim. Acta* **2001**, *47*, 599.